npj | 2D materials and applications

Article

Published in partnership with FCT NOVA with the support of E-MRS

https://doi.org/10.1038/s41699-024-00488-3

Probing the interplay of interactions, screening and strain in monolayer MoS_2 via self-intercalation

Borna Pielić[1,2] ✉, Matko Mužević[3], Dino Novko[2], Jiaqi Cai[1], Alice Bremerich[1], Robin Ohmann[1], Marko Kralj[2], Iva Šrut Rakić[2] ✉ & Carsten Busse[1]

Controlling many-body interactions in two-dimensional systems remains a formidable task from the perspective of both fundamental physics and application. Here, we explore remarkable electronic structure alterations of MoS_2 monolayer islands on graphene on Ir(111) induced by non-invasive self-intercalation. This introduces significant differences in morphology and strain of MoS_2 as a result of the modified interaction with the substrate. Consequently, considerable changes of the band gap and non-rigid electronic shifts of valleys are detected, which are a combined effect of the screening of the many-body interactions and strain in MoS_2. Furthermore, theory shows that each substrate leaves a unique stamp on the electronic structure of two-dimensional material in terms of those two parameters, restricted by their correlation.

Two-dimensional (2D) materials demonstrate remarkable potential for future electronic and optoelectronic devices[1–4]. However, their atomic thickness renders them highly sensitive to environmental conditions[5–8]. Structural defects, the selection of the substrate, the intercalation of foreign atomic species, and electromagnetic fields are common tools used for altering the intrinsic interactions and properties of 2D materials[9–12]. Specifically, the selection of the substrate is as crucial as the 2D material itself. Key effects of the substrate are dielectric screening of the many-body interactions[5,13] and strain of the crystal lattice of the 2D material[14,15]. The first one is caused by charge polarization in the substrate in response to the charges in the 2D material, while the second reflects the need to find a lattice parameter that optimizes in-plane and out-of-plane bonding simultaneously. Simplistically, these mechanisms are often studied individually. Dielectric screening was especially in focus of research[16–20] and it produces rigid band shifts, i.e. $\Delta E(\vec{k}) = \text{const}$[5]. The reality is that each combination of 2D material and substrate possesses a screening-strain combination that puts a unique signature on its electronic structure.

A suitable system for studying the influence of the substrate are semiconducting transition metal dichalcogenides (TMDs) whose multivalley electronic structure[21] is especially strain-sensitive[22–24]. Controlling changes in their valley profiles is crucial for fundamental electronic structure design and various physical properties such as carrier mobility[25], optical response and band gap[22,25–27], as well as superconductivity[28]. While theory suggests that the lattice strain causes non-rigid shifts of both valence and conduction band, i.e. $\Delta E(\vec{k}) \neq$ const., it remains experimentally unclear how the valley profiles are influenced by the substrate. A strong interaction, as found for metallic substrates, can cause significant reduction of the band gap[19,29], as well as quenching of the ordered states such as superconductivity[30] and charge density waves[31]. A weak interaction, as present in the case of van der Waals (vdW) substrates, is believed to conserve the intrinsic properties[28,32,33], even though there are instances where a vdW substrate induces inevitable modifications to the electronic structure $E(\vec{k})$ (e.g., band gap) and optical properties (e.g., exciton energy)[5,18]. Naively, the interaction between two stacked 2D materials is usually assumed to be vdW-type only, while covalent-like bonding is mostly considered when 2D materials are grown on metal substrates[34,35]. It is therefore of utmost importance to characterize the interaction with the substrate and comprehend its correlation with the electronic structure of the TMD. Current analyses, predominantly relying on angle-resolved photoemission spectroscopy (ARPES)[5,19,36] to track the valence band (VB) and optical spectroscopy to monitor the optical (excitonic) band gap, can provide only incomplete insights, whereas comprehensive studies addressing modifications in both the VB and conduction bands (CB) through techniques like scanning tunneling spectroscopy (STS) are infrequent[37].

Here, we go beyond these studies and utilize STS to investigate valley profile and binding modifications in semiconducting MoS_2 on graphene (Gr) on Ir(111), induced by self-intercalation, the intercalation of native atoms of the 2D material between Gr and its substrate (e.g. Mo and S for MoS_2). Intercalated S weakens the interaction in the 2D stack, while Mo strengthens it, changing the contribution of the covalent-like bonding between the layers. Such substrate alterations through self-intercalation

[1]Department Physik, Universität Siegen, Walter-Flex-Str. 3, 57068 Siegen, Germany. [2]Centre for Advanced Laser Techniques, Institute of Physics, Bijenička cesta 46, 10000 Zagreb, Croatia. [3]Department of Physics, Josip Juraj Strossmayer University of Osijek, Trg Ljudevita Gaja 6, Osijek, 31000, Croatia.
✉e-mail: borna.pielic@uni-siegen.de; isrut@ifs.hr

affect the screening of many-body interactions (rigid shits of the bands), as well as strain that is signatured as the non-rigid shifts of both VB and CB. The present study shows and unravels how to engineer electronic structure and bonding within the 2D stack in a prudent and controllable way.

Results

MoS_2 on Gr/Ir(111), grown by molecular beam epitaxy (MBE), is known as quasi-freestanding[38], as the electronic band structure remains almost undisturbed[39]. To modify the environment of MoS_2 by self-intercalation, we have fine-tuned the synthesis recipe to achieve either full S or Mo intercalation (see Methods). This is elegant because a modification of the substrate is embedded into the synthesis procedure, and it is also non-invasive, as the stoichiometry of the MoS_2/Gr stack stays intact.

Growth with a large excess of S leads to irregular MoS_2 monolayer islands on S-intercalated Gr, as shown by scanning tunneling microscopy (STM) in Fig. 1a–d. Low energy electron diffraction (LEED) displays diffraction arcs of MoS_2, indicating imperfect epitaxial alignment (Fig. 1b). The islands appear joined together from regular smaller segments, often with clear boundaries between them. This morphology is similar to the one found for MoS_2/Gr/Ir(111) in a detailed growth study[38], where it was attributed to diffusion and aggregation of islands during the annealing step (Smoluchowski ripening). S intercalation is evident from decorated domain boundaries visible through Gr in STM (white arrow in Fig. 1a), and c(4 × 2) diffraction spots in LEED (yellow spots in Fig. 1b)[40]. Lattice constants of MoS_2 and Gr obtained from LEED are $a^{S}_{MoS_2} = (3.15 \pm 0.01)$ Å and $a^{S}_{Gr} = (2.462 \pm 0.004)$ Å. The STM height profile and schematic sectional view (Fig. 1c, d) represent the side view of the sample.

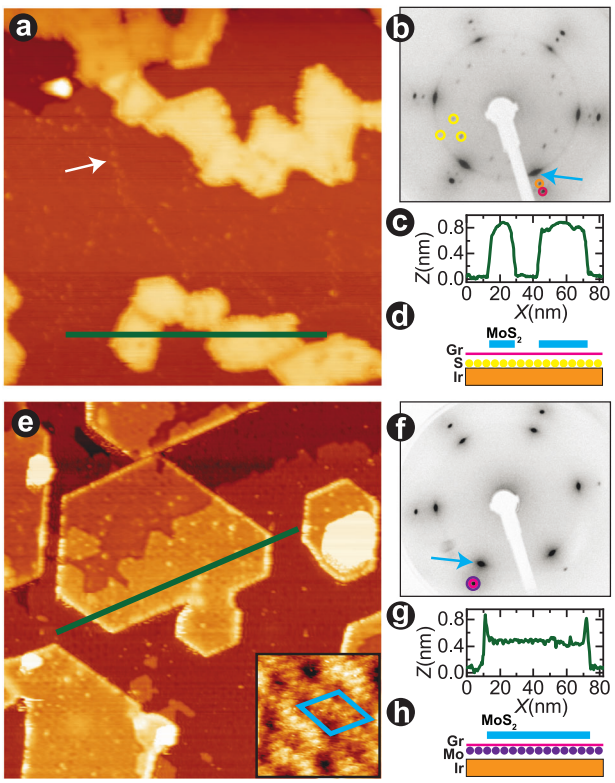

Fig. 1 | Structural characterization. STM images of MoS_2/Gr/S/Ir(111) (**a**) and MoS_2/Gr/Mo/Ir(111) (**e**). Inset in (**e**): atomically resolved image, blue: moiré unit cell. LEED patterns (**b**, **f**) of samples shown in (**a**, **e**): superposition of spots from Ir(111) (one marked by an orange circle), Gr (magenta), Mo (purple), S (yellow) and MoS_2 (arrow). STM line profiles (**c**, **g**) and schematic sectional views (**d**, **h**) along green lines in (**a**, **e**) that display arrangement of Ir, Gr, Mo, S and MoS_2. The edges and grain boundaries in both (**a**) and (**e**) have different contrast compared to the inner part of the islands, due to their 1D states[59,63]. Note that the apparent height of MoS_2 islands in STM is bias-dependent, in line with the previous report[64]. U_t, I_t: (**a**) 1.4 V, 0.1 nA, (**e**) − 1.3 V, 0.2 nA, inset − 1.3 V, 0.2 nA. Image size: (**a**, **e**) 120 nm × 120 nm, (inset) 4 nm × 4 nm. Electron beam energy: (**b**) 96 eV, (**f**) 73 eV.

Growth with an excess of Mo leads to large hexagonal MoS_2 monolayer islands on a fully Mo-intercalated Gr, as revealed by STM in Fig. 1e. The LEED pattern in Fig. 1f shows sharp MoS_2 spots, which confirms strong epitaxy between MoS_2 and Gr[38]. The absence of additional diffraction spots due to intercalation shows that Mo atoms are in registry with Gr (similarly to Cs intercalation[41]), i.e. a 1 × 1 superstructure. Figure 1g shows a line profile and 1h the corresponding schematic sectional view. The lattice constants determined from LEED are $a^{Mo}_{MoS_2} = (3.20 \pm 0.03)$ Å and $a^{Mo}_{Gr} = (2.465 \pm 0.004)$ [see Supplementary Information (SI)]. Evidently, the lattice constant of MoS_2 has significantly increased. Apart from the atomic lattice of MoS_2, another hexagonal superstructure with a periodicity of (11.0 ± 0.5) Å is observed on MoS_2 (see inset in Fig. 1e), which is the moiré superstructure arising from the superposition of Gr and MoS_2 (see SI).

The different morphologies of the two samples in Fig. 1 are attributed to a difference in the binding between MoS_2 and Gr: For MoS_2/Gr/S/Ir(111), Smoluchowski ripening and scattering in epitaxial alignment indicate a relatively weak interaction between Gr and MoS_2. Absence of island mobility, good epitaxy, as well as the appearance of a moiré pattern between Gr and MoS_2, indicate that the interaction is stronger for the case of Mo intercalation.

To quantify the interaction between MoS_2 and Gr depending on self-intercalation or without, we perform density functional theory (DFT) calculations (for details see Methods). The charge density difference, visualized in Fig. 2a–c, represents the charge redistribution after adding the MoS_2 to the rest of the stack. For the non-intercalated sample (Fig. 2a), a prominent accumulation of negative charge at the lower S atoms of MoS_2 and charge depletion at the C atoms are determined. This polarization of the charge is weaker when S is intercalated below Gr, while for Mo intercalation it is significantly stronger. On the same footing, the layer separation (quantified by the distance between Gr and the lower S atoms in Fig. 2a–c) increases when going from the non-intercalated to the S-intercalated system, and reduces for Mo intercalation. A quantitative measure for the strength of the interaction is the adsorption energy[42] of MoS_2 per unit cell. The calculated values, 0.22 eV (none), 0.20 eV (S), and 0.32 eV (Mo), reflect the general tendency that higher adsorption energies lead to smaller separations (Fig. 2d). Redistributed charge indicates that the bonding between MoS_2 and Gr goes beyond vdW interaction, i.e. comprises covalent-like bonding, which is most prominent in the case of Mo intercalation. Furthermore, Fig. 2e shows that a larger total accumulated charge (at the lower S and C atoms) is correlated with a higher adsorption energy of MoS_2.

The DFT calculations yield 3.15 Å for the lattice constant of freestanding MoS_2, which is in line with the one measured for the MoS_2 on Gr/S/Ir(111). Therefore, we consider MoS_2 as unstrained in this case. Following this reasoning, MoS_2 is compressed by ~ − 0.6 % in the absence of intercalation ($a_{MoS_2} = 3.13$ Å[38]), while Mo intercalation introduces a stretching of ~ + 1.6 %. Apparently, the strain (ϵ) in MoS_2 is introduced by the substrate and the strain energy ($\sim \epsilon^2$) is in strong correlation with the adsorption of MoS_2, as shown in Fig. 2f. In general, the lattice constant results from a compromise between minimization of elastic energy (the overlayer wants to keep the lattice constant of the freestanding case) and maximization of binding energy (the overlayer wants to adjust to the substrate). While a comprehensive description is complex and depends on the details of the individual systems (for the non-intercalated case see ref. 38), it is straightforward to see that the system is willing to pay more elastic energy when the interaction is stronger, as visible in Fig. 2f. In this case, we even find a higher-order commensurability between MoS_2 and Gr of (10 × 10)/(13 × 13). It is a general effect that ultrathin materials can adjust to their substrates, even commensurate-incommensurate transitions have been observed within 2D stacks[43], but so far not for MoS_2.

We now examine the electronic structure of MoS_2/Gr/S/Ir(111) and MoS_2/Gr/Mo/Ir(111) using STS. All spectra were taken far away from edges and defects, as well as averaged among different areas (see Methods for more details). We include the data representing the non-intercalated sample[39] for comparison. Figure 3a shows the dI/dU spectra that strongly

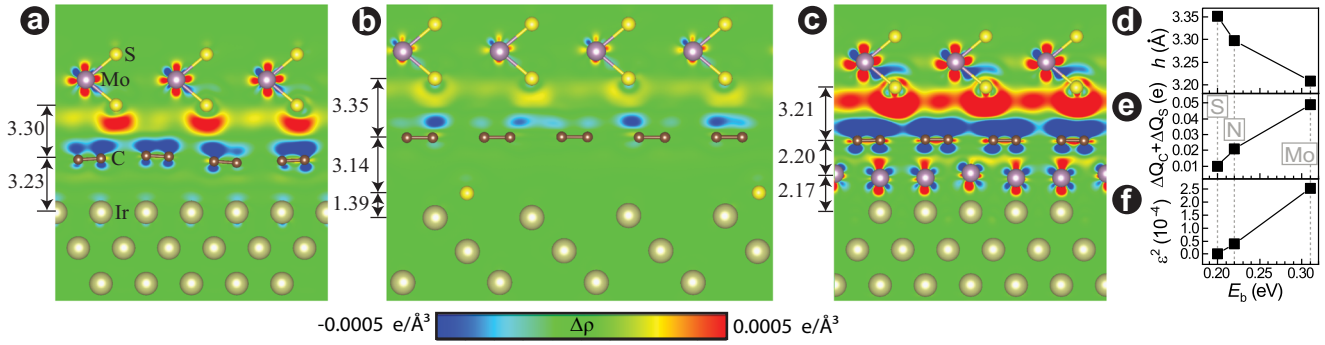

Fig. 2 | DFT calculations. DFT structure model (side view) and the charge density difference for (**a**) MoS_2/Gr/Ir(111), (**b**) MoS_2/Gr/S/Ir(111) and (**c**) MoS_2/Gr/Mo/Ir(111). Legend indicates the colors ranging from charge depletion to charge accumulation (in units of the electron charge $e \approx -1.6 \times 10^{-19}$C). Dependence of adsorption energy of MoS_2 on layer separation (**d**), accumulated charge on C and lower S atom (**e**), and ϵ^2 (**f**). Dashed gray lines in (**d**–**f**) are visual aid for 3 systems: S (S-intercalated), N (Non-intercalated), and Mo (Mo-intercalated).

depend on the local density of states and can directly be compared with the calculated band structures in Fig. 3b. Local maxima/minima in $E(k)$ are expected to lead to peaks in dI/dU. In addition, one has to take into account that states close to Γ are enhanced in STS as their vanishing parallel crystal momentum strongly favours the tunnelling process[39,44]. Because of this, we attribute the pronounced peak at negative U to the state in Γ, as reported before[39]. The first peak for positive U is interpreted as the conduction band minimum at K (here, there are no competing states with smaller parallel crystal momentum), while the second, more pronounced peak is attributed to the local minimum at the Q point. Our association of the peaks in STS spectra with the electronic states is consistent with earlier studies on similar systems[37,39,45]. We use the difference between the peaks labeled Γ and K as a quantitative measure of the band gap ($E_{\Gamma-K}$). For S intercalation, the band gap ($E^{S}_{\Gamma-K} = 2.62 \pm 0.03$ eV) is in line with the value for the non-intercalated sample ($E_{\Gamma-K} = 2.63$ eV[39]), while for Mo intercalation it is significantly reduced ($E^{Mo}_{\Gamma-K} = 2.20 \pm 0.02$ eV). Moreover, S intercalation shifts the band gap downwards. Looking separately at valence and conduction bands, E_{Γ} is shifted down for S intercalation and up for Mo intercalation. Since the state in Γ has an out-of-plane character it is carrying information on the interlayer interaction between MoS_2 and Gr, as evidenced by tuning the twisting angle between two MoS_2 layers[46]. Similarly, an increased interaction between MoS_2 and Gr in our case, is signalled as an up-shift of Γ. The shifts in the conduction band are more complex. Namely, for both S and Mo intercalation the K point is shifted down, while Q is shifted up for Mo intercalation and down for S intercalation. In total, this results in a pronounced change of the energy difference between the states in Q and K (E_{K-Q}), starting from $E^{non}_{K-Q} = 0.13 \pm 0.05$ eV for the non-intercalated sample[39] to $E^{S}_{K-Q} = 0.21 \pm 0.03$ eV for S intercalation and even $E^{Mo}_{K-Q} = 0.46 \pm 0.02$ eV for Mo intercalation (Fig. 3a).

The obtained results show that the electronic band structure of MoS_2 can be significantly tailored, even though in all three cases the substrate is Gr, but subtly modified. However, even such fine tuning of the dielectric environment does not allow us to distinguish the impact of dielectric screening and strain on electronic band structure, as they are interconnected. Changing the substrate for a 2D material in general can therefore be looked as turning two knobs at the same time, i.e. dielectric screening of the many-body interaction and strain of the crystal lattice of the 2D material. Independent change of these parameters can only be studied theoretically.

To understand the measured modifications of the band structure, we performed DFT calculations for freestanding MoS_2 with a variation of dielectric screening and strain. The common PBE functional does not fully include the short-range exchange interaction between electrons. This is important, as the total range of the exchange interaction for insulators exponentially decreases with the value of the band gap[47]. Otherwise, calculations result in an overestimated screening, and therefore underestimate the band gap[48]. The exchange interaction can be substituted by mixing the PBE functional with the Hartree-Fock approximation which performs the exact exchange (PBE0 hybrid functional[49]). However, for the inspection of the screening, it is necessary to apply the HSE functional which enables varying the inverse screening length ω (for $\omega \to 0$, HSE → PBE0, and for $\omega \to \infty$, HSE → PBE)[50]. This parameter, analogous to the Thomas-Fermi screening wavevector k_{TF}, provides a physical basis for our calculations[51]. The intrinsic dielectric screening, and therefore intrinsic ω, can be obtained from the dielectric function ε_{MoS_2} of freestanding MoS_2. In the presence of a substrate, the modified dielectric screening could be modelled with an effective dielectric function such as $\varepsilon_{eff} = 1 - (1 + \frac{1-\varepsilon_{sub}}{1+\varepsilon_{sub}} e^{-2qd})(1 - \varepsilon_{MoS_2})$, where ε_{sub} denotes the dielectric function of the bare substrate, d is the distance between MoS_2 and the substrate, and q is the momentum of the charge carriers[52,53]. Even though one could consider the dielectric screening from the substrate in MoS_2 by calculating ω from ε_{eff}, here the different substrate screening is mimicked by simply varying the value of ω. This phenomenological approach avoids computational complexity associated with the exact dielectric functions calculations, while still enabling a qualitative comparison with the experimental results[54].

Along with the screening, we also strain the in-plane lattice constant of MoS_2, which affects the electronic structure in a dramatic way (see Fig. 3b). On the one hand, an increase of the screening from $\omega = 0$ to $\omega = 0.12$ for a fixed lattice constant, results in a reduction of the band gap, while the topology of the bands is almost unchanged. On the other hand, the increase of the lattice constant from 3.13 to 3.23 Å with a fixed screening, results in significant relative shifts between the valleys in both conduction and valence band. Namely, the energy difference between the K and Q valleys in the CB increases with lattice constant, while the one between Γ and K in the VB decreases. This is manifested as the transition of the VB maximum from K to Γ for 3.23 Å. In the band structure calculated for 3.20 Å, which corresponds to experimentally obtained MoS_2 intercalated by Mo, the band gap is still direct but the K and Γ valleys are very close in energy. The possibility to switch the nature of the band gap just by substrate intercalation is very important in the context of applications, and we believe that our research will spark further exploration in this field.

For better visualization of the influence of screening and strain effects on the $E_{\Gamma-K}$ and E_{K-Q}, we extract the results in 2D ω-a maps shown in Fig. 3c, d. The upper map presents $E_{\Gamma-K}$ being a highly affected by both strain and screening, and having maximal value for the smallest lattice constant in the absence of screening. Contrary to that, E_{K-Q}, presented in the lower panel, shows strong dependence on the lattice constant, and fairly weak dependence on screening.

For comparison, theoretical and experimental values of $E_{\Gamma-K}$ and E_{K-Q} for the three measured lattice constants are represented as a histogram in Fig. 3e, f. The trend of both energies agrees with the experiment (for proper visual comparison, one needs to take into account different dielectric screening), thus proving that DFT calculations with HSE functional can credibly describe the influence of strain and screening in a 2D semiconductor.

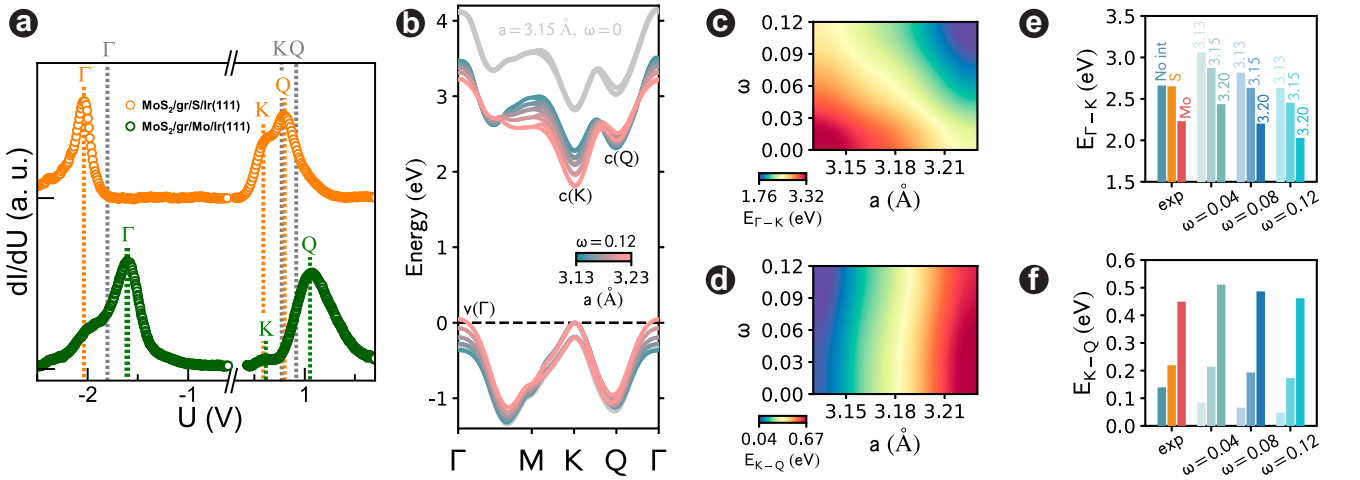

Fig. 3 | Electronic band structure. a STS characterization of MoS_2 intercalated by S (orange) and Mo (green). The values of the critical energy points Γ, Q and K for S (Mo) intercalation are summarized in Supplementary Table 1. The ticks on the dI/dU-axis depict the dI/dU = 0 for the two spectra shown. The values for the non-intercalated sample (dashed gray lines) are from ref. 39 (**b**) DFT band structure for freestanding MoS_2 calculated for two values of screening and five lattice constants. **c**, **d** Color maps for the energy differences $E_{\Gamma-K}$ and E_{K-Q} obtained by interpolation of a 5 × 5 set of the energy values and ω-a coordinates. **e**, **f** Histograms with $E_{\Gamma-K}$ and E_{K-Q} values, displaying that the trend of both energies agrees between experiment and theory. The values of the lattice constants are shown in Å. The lattice constant of MoS_2 for the non-intercalated sample is taken from ref. 38.

Naively, the match between $E_{\Gamma-K}$ and $E^{S}_{\Gamma-K}$ could be attributed to similar screening. However, one has to take the significant compression of MoS_2 on Gr/Ir(111) (as evidenced by LEED) into account: Compression of the TMD lattice constant increases the band gap, as shown by Fig. 3c. This has to be counteracted by stronger screening which reduces the band gap (Fig. 3c). It follows that the many-body interaction in MoS_2 on Gr/Ir(111) is screened stronger than on Gr/S/Ir(111). Conversely, both screening and strain are reducing the band gap of MoS_2 in case of Mo intercalation, thus resulting in the smallest band gap.

Discussion

These observations can help us expand our understanding of the dielectric engineering of 2D heterostructures and open new avenues to control and tailor the matter and corresponding physical properties. Namely, recent Raman measurements revealed strong connection between enhancement of the electron-phonon interactions in TMDs and valley profiles of CB and VB[26]. Also, heat transfer, carrier relaxation, and exciton-phonon scattering clearly depend on the energy position of valleys in TMDs[5,55,56]. Self-intercalation of multi-valley heterostructure can therefore be used to explore different regimes of transport, carrier thermalization, exciton binding, and superconductivity.

In conclusion, Gr modified by either S or Mo intercalation acts as effectively different substrates for MoS_2 in these two cases, which is evident from differences in morphology and strain of MoS_2. We conclude that the Mo intercalation results in strengthening of the interaction between MoS_2 and Gr, while S intercalation results in weakening. The interaction with the buffer layer has a strong correlation with the strain present in MoS_2. Furthermore, strain of the lattice and screening of the many-body interactions have shown to have a complex and interdependent impact on the electronic structure of MoS_2. The strength of any of these interactions in 2D stacks, as well as their mutual correlation, are setting inevitable constraints on design and performance of potential devices. Our results will pave the way for new studies and help deepen research on 2D systems with enhanced correlations, especially on novel multivalley semiconductors and superconductors.

Methods

Experimental methods

Ir(111) was cleaned by cycles of Ar ion sputtering (1.5 keV) and flash-annealing to 1500 K. Sample cleanliness was checked and confirmed by low energy electron diffraction (LEED) and scanning tunneling microscopy (STM). Graphene on Ir(111) was prepared by a cycle of temperature programmed growth (TPG), followed by chemical vapor deposition (CVD)[57]. Epitaxial growth of MoS_2 monolayer islands is done by applying two growth procedures: (1) A two-step molecular beam epitaxy (MBE) process which results in S being intercalated between Gr and Ir(111), and (2) a single-step MBE process resulting in Mo intercalation.

Two-step MBE: In the growth step, the sample is exposed to a Mo flux $F^{Mo} = 9 \times 10^{15}$ m^{-2}s^{-1} (determined by depositing Mo onto bare Ir(111) and analyzing the coverage of Mo islands in a 1000 × 1000 nm^2 area) and S pressure $p^S = 5 \times 10^{-6}$ mbar at room temperature for 440 s. A high S flux is provided by a valved sulfur source (VSS). In an annealing step, the sample is flash-annealed to 1030 K with continuous exposure to the same S pressure. Full intercalation of S [c(4 × 2) superstructure] is achieved by applying the relatively high S pressure during both growth and annealing step. This results in irregular MoS_2 islands ($\Theta^{MoS_2} = 0.21$ ML), as shown by the STM image in Fig. 1a. Islands are composed of segments (average diameter ≈ 20 nm) that are separated by grain boundaries.

One-step MBE: The sample is exposed to $F^{Mo} = 4.5 \times 10^{16}$ m^{-2}s^{-1} and $p^S = 2.5 \times 10^{-5}$ mbar at 1030 K. To be able to grow MoS_2 at the high substrate temperatures needed for effective Mo-intercalation, we need even higher S flux than in the two-step MBE. Note that the high temperature used here corresponds to the annealing temperature in the two-step MBE. Moreover, the ratio between S pressure and Mo flux (p^S/F_{Mo}) was kept the same. MoS_2 flakes have an average diameter of ≈ 44 nm. Graphene was fully intercalated by Mo, while the remaining material formed the MoS_2 flakes ($\Theta^{MoS_2} = 0.64$ ML).

The lattice constants of MoS_2 and Gr are measured with respect to the Ir(111) lattice constant ($a_{Ir(111)} = 2.715$ Å[58]).

Scanning tunneling spectroscopy (STS) measurements were done in constant current mode at 120 K. STS is performed using a lock-in amplifier with frequency 3413 Hz and 20 mV modulation voltage. The presence of metallic edges, grain boundaries, point defects, imperfections of intercalation, and step edges make our samples electronically diverse. For example, an upward band bending is noticed near (<5 nm) to the metallic edges and point defects, in line with previous findings for similar systems[37,59]. Therefore, to exclude any contributions to the spectrum arising from such areas, all spectra were recorded at least 10 nm away. We used a tungsten tip, whose termination was done by multiple bias voltage pulses, until the most prominent electronic feature (state in the Γ point) was consistently recorded at the same energy. Stabilization voltage of the spectra recorded in the negative (positive)

bias voltage range was −2.5 V (2 V), and stabilization current was always 0.1 nA.

Theoretical methods

To calculate adsorption energy (E_b) and charge density difference, we have used two different hexagonal supercells, as the symmetry of the c(4 × 2) S intercalation and Mo intercalation is different. The supercell that was used for the Mo intercalated and the non-intercalated system consisted of 3 × 3 unit cells of MoS_2 (9 Mo and 18 S atoms), 4 × 4 unit cells of graphene (32 C atoms) and 3 layers of Ir(111) (36 Ir atoms), with an additional layer of 9 Mo atoms between graphene and Ir(111) for Mo intercalation. The supercell used for the S intercalated system consisted of 4 × 4 unit cells of MoS_2 (16 Mo and 32 S atoms), 5 × 5 unit cells of graphene (50 C atoms), a layer of intercalated S atoms (8 S atoms) and 3 layers of Ir(111) (48 atoms). The calculation for the non-intercalated system was repeated with this lattice, and no change in the adsorption energy was observed. The lattice constants of supercells (9.57 and 12.76 Å) were chosen in a way that minimizes the strain on MoS_2, while graphene and Ir(111) are strained (− 2.3% and 1.5% for the smaller superlattice, 4% and 17% for the larger one)[60]. To eliminate the interaction between periodic images in the perpendicular direction, the hexagonal lattice constant was set to at least 31 Å. The coordinates of MoS_2, graphene and intercalated atoms were free to relax during structure optimization, while the Ir(111) x and y coordinates were fixed. The adsorption energy was calculated by

$$E_b = \frac{1}{N}\left(E_{tot} - E_{MoS_2} - E_{rest}\right), \quad (1)$$

where E_{tot} is the energy of the entire system, E_{MoS_2} is the energy of the isolated MoS_2 layer, E_{rest} is the energy of the system without MoS_2 and N is the number of MoS_2 unit cells in the system. The ground state electronic structure calculations of the heterostructures MoS_2/Gr/Ir, MoS_2/Gr/Mo/Ir, and MoS_2/Gr/S/Ir were performed by means of the plane-wave density-functional-theory (DFT) code Quantum Espresso[61]. All calculations were done using the plane wave cutoff energy set to 1360 eV (100 Ry) and 5 × 5 × 1 Monkhorst-Pack k-point mesh. To correctly include the non-local dispersion forces between different subsystems of heterostructures, the exchange correlation potential was approximated by the vdW-DF-cx functional[62].

To accurately describe the band gap and dispersion of electronic states of isolated MoS_2 single layer presented in Fig. 3 of the main text, we adopt the HSE xc functional[55]. Here, a 24 × 24 × 1 Monkhorst-Pack grid was used for sampling the Brillouin zone (with Marzari-Vanderbilt smearing of 0.008 Ry), and a q grid of 12 × 12 × 1 for sampling the Fock operator. We also include the spin-orbit coupling.

Data availability

The authors affirm that all data underpinning the study's conclusions are presented within the manuscript and its supplementary materials. Moreover, additional data can be made available by the corresponding authors upon reasonable request.

Received: 15 February 2024; Accepted: 18 July 2024;
Published online: 12 September 2024

References

1. Lemme, M. C., Akinwande, D., Huyghebaert, C. & Stampfer, C. 2D materials for future heterogeneous electronics. *Nat. Commun.* **13**, 1392 (2022).
2. Cheng, J., Wang, C., Zou, X. & Liao, L. Recent advances in optoelectronic devices based on 2D materials and their heterostructures. *Adv. Opt. Mater.* **7**, 1800441 (2019).
3. Hu, W. & Yang, J. Two-dimensional van der Waals heterojunctions for functional materials and devices. *J. Mater. Chem. C* **5**, 12289–12297 (2017).
4. Liu, Y., Zhang, S., He, J., Wang, Z. M. & Liu, Z. Recent progress in the fabrication, properties, and devices of heterostructures based on 2D materials. *Nano-Micro Lett.* **11**, 13 (2019).
5. Waldecker, L. et al. Rigid band shifts in two-dimensional semiconductors through external dielectric screening. *Phys. Rev. Lett.* **123**, 206403 (2019).
6. Zhang, C. et al. Probing critical point energies of transition metal dichalcogenides: Surprising indirect gap of single layer WSe_2. *Nano Lett.* **15**, 6494–6500 (2015).
7. Holbrook, M. et al. Creating a nanoscale lateral junction in a semiconductor monolayer with a large built-in potential. *ACS Nano* **17**, 6966–6972 (2023).
8. Nguyen, P. V. et al. Visualizing electrostatic gating effects in two-dimensional heterostructures. *Nature* **572**, 220–223 (2019).
9. Chen, Q., Zhu, L., Guo, J., Zhou, J. & Sun, Z. Energetic and kinetic coupling between the intercalated atom and intrinsic S vacancy in the MoS_2 bilayer. *J. Phys. Chem. C* **126**, 18560–18570 (2022).
10. Zhou, B. et al. A chemical-dedoping strategy to tailor electron density in molecular-intercalated bulk monolayer MoS_2. *Nat Synth.* **3**, 67–75 (2023).
11. Twitto, A. et al. Optoelectronics of atomic metal-semiconductor interfaces in tin-intercalated MoS_2. *ACS Nano* **16**, 17080–17086 (2022).
12. Stern, C. et al. Enhancing light-matter interactions in MoS_2 by copper intercalation. *Adv. Mater.* **33**, 2008779 (2021).
13. Drüppel, M., Deilmann, T., Krüger, P. & Rohlfing, M. Diversity of trion states and substrate effects in the optical properties of an MoS_2 monolayer. *Nat. Commun.* **8**, 2117 (2017).
14. Conley, H. J. et al. Bandgap engineering of strained monolayer and bilayer MoS_2. *Nano Lett.* **13**, 3626–3630 (2013).
15. Herbig, C. et al. Local electronic properties of coherent single-layer WS_2/WSe_2 lateral heterostructures. *Nano Lett.* **21**, 2363–2369 (2021).
16. Sharma, M., Kumar, A., Ahluwalia, P. K. & Pandey, R. Strain and electric field induced electronic properties of two-dimensional hybrid bilayers of transition-metal dichalcogenides. *J. Appl. Phys.* **116**, 063711 (2014).
17. Stier, A. V. et al. Probing the influence of dielectric environment on excitons in monolayer WSe_2: insight from high magnetic fields. *Nano Lett.* **16**, 7054–7060 (2016).
18. Raja, A. et al. Coulomb engineering of the bandgap and excitons in two-dimensional materials. *Nat. Commun.* **8**, 15251 (2017).
19. Ugeda, M. M. et al. Giant bandgap renormalization and excitonic effects in a monolayer transition metal dichalcogenide semiconductor. *Nat. Mater.* **13**, 1091–1095 (2014).
20. Andersen, K., Latini, S. & Thygesen, K. S. Dielectric genome of van der Waals heterostructures. *Nano Lett.* **15**, 4616–4621 (2015).
21. Sohier, T. et al. Valley-engineering mobilities in two-dimensional materials. *Nano Lett.* **19**, 3723–3729 (2019).
22. Ortenzi, L., Pietronero, L. & Cappelluti, E. Zero-point motion and direct-indirect band-gap crossover in layered transition-metal dichalcogenides. *Phys. Rev. B* **98**, 195313 (2018).
23. Yuan, H. et al. Evolution of the valley position in bulk transition-metal chalcogenides and their monolayer limit. *Nano Lett.* **16**, 4738–4745 (2016).
24. Blundo, E. et al. Strain-tuning of the electronic, optical, and vibrational properties of two-dimensional crystals. *Appl. Phys. Rev.* **8**, 021318 (2021).
25. Sohier, T. et al. The impact of valley profile on the mobility and Kerr rotation of transition metal dichalcogenides. *2D Mater.* **10**, 025006 (2023).
26. Sohier, T. et al. Enhanced electron-phonon interaction in multivalley materials. *Phys. Rev. X* **9**, 031019 (2019).
27. Chaves, A. et al. Bandgap engineering of two-dimensional semiconductor materials. *npj 2D Mater. Appl.* **4**, 29 (2020).
28. Ding, D. et al. Multivalley superconductivity in monolayer transition metal dichalcogenides. *Nano Lett.* **22**, 7919–7926 (2022).

29. Bruix, A. et al. Single-layer MoS_2 on Au(111): band gap renormalization and substrate interaction. *Phys. Rev. B* **93**, 165422 (2016).
30. Lu, J. et al. Full superconducting dome of strong Ising protection in gated monolayer WS_2. *Proc. Natl. Acad. Sci. USA* **115**, 3551–3556 (2018).
31. Sanders, C. E. et al. Crystalline and electronic structure of single-layer TaS_2. *Phys. Rev. B* **94**, 081404 (2016).
32. Hall, J. et al. Environmental control of charge density wave order in monolayer 2H-TaS_2. *ACS Nano* **13**, 10210–10220 (2019).
33. Lasek, K. et al. Synthesis and characterization of 2D transition metal dichalcogenides: Recent progress from a vacuum surface science perspective. *Surf. Sci. Rep.* **76**, 100523 (2021).
34. Busse, C. et al. Graphene on Ir(111): Physisorption with chemical modulation. *Phys. Rev. Lett.* **107**, 036101 (2011).
35. Miwa, J. A. et al. Electronic structure of epitaxial single-layer MoS_2. *Phys. Rev. Lett.* **114**, 046802 (2015).
36. Katoch, J. et al. Giant spin-splitting and gap renormalization driven by trions in single-layer WS_2/h-BN heterostructures. *Nat. Phys.* **14**, 355–359 (2018).
37. van Efferen, C. et al. Metal-insulator transition in monolayer MoS_2 via contactless chemical doping. *2D Mater.* **9**, 025026 (2022).
38. Hall, J. et al. Molecular beam epitaxy of quasi-freestanding transition metal disulphide monolayers on van der Waals substrates: a growth study. *2D Mater.* **5**, 025005 (2018).
39. Murray, C. et al. Comprehensive tunneling spectroscopy of quasifreestanding MoS_2 on graphene on Ir(111). *Phys. Rev. B* **99**, 115434 (2019).
40. Pielić, B. et al. Sulfur structures on bare and graphene-covered Ir(111). *J. Phys. Chem. C* **124**, 6659–6668 (2020).
41. Petrović, M. et al. The mechanism of caesium intercalation of graphene. *Nat. Commun.* **4**, 2772 (2013).
42. Chakarova-Käck, S. D., Schröder, E., Lundqvist, B. I. & Langreth, D. C. Application of van der Waals density functional to an extended system: Adsorption of benzene and naphthalene on graphite. *Phys. Rev. Lett.* **96**, 146107 (2006).
43. Woods, C. R. et al. Commensurate-incommensurate transition in graphene on hexagonal boron nitride. *Nat. Phys.* **10**, 451–456 (2014).
44. Feenstra, R., Stroscio, J. A. & Fein, A. Tunneling spectroscopy of the Si(111)2 × 1 surface. *Surf. Sci.* **181**, 295–306 (1987).
45. Pielić, B. et al. Electronic structure of quasi-freestanding WS_2/MoS_2 heterostructures. *ACS Appl. Mater. Interfaces* **13**, 50552–50563 (2021).
46. Wang, Z., Chen, Q. & Wang, J. Electronic structure of twisted bilayers of graphene/MoS_2 and MoS_2/MoS_2. *J. Phys. Chem. C* **119**, 4752–4758 (2015).
47. Kohn, W. Density functional theory for systems of very many atoms. *Int. J. Quantum Chem.* **56**, 229–232 (1995).
48. Kuc, A., Zibouche, N. & Heine, T. Influence of quantum confinement on the electronic structure of the transition metal sulfide TS_2. *Phys. Rev. B* **83**, 245213 (2011).
49. Ernzerhof, M., Perdew, J. P. & Burke, K. Coupling-constant dependence of atomization energies. *Int. J. Quantum Chem.* **64**, 285–295 (1997).
50. Heyd, J., Scuseria, G. E. & Ernzerhof, M. Hybrid functionals based on a screened Coulomb potential. *J. Chem. Phys.* **118**, 8207–8215 (2003).
51. Yang, J., Falletta, S. & Pasquarello, A. Range-separated hybrid functionals for accurate prediction of band gaps of extended systems. *npj Comput. Mater.* **9**, 108 (2023).
52. Despoja, V. et al. Strong acoustic plasmons in chemically doped graphene induced by a nearby metal surface. *Phys. Rev. B* **100**, 195401 (2019).
53. Zibouche, N., Schlipf, M. & Giustino, F. GW band structure of monolayer MoS_2 using the SternheimerGW method and effect of dielectric environment. *Phys. Rev. B* **103**, 125401 (2021).
54. Nilforoushan, N. et al. Photoinduced renormalization and electronic screening of quasi-two-dimensional Dirac states in $BaNiS_2$. *Phys. Rev. Res.* **2**, 043397 (2020).
55. Bae, S. et al. K-point longitudinal acoustic phonons are responsible for ultrafast intervalley scattering in monolayer $MoSe_2$. *Nat. Commun.* **13**, 4279 (2022).
56. Aslan, B. et al. Strained bilayer WSe_2 with reduced exciton-phonon coupling. *Phys. Rev. B* **101**, 115305 (2020).
57. Coraux, J. et al. Growth of graphene on Ir(111). *New J. Phys.* **11**, 023006 (2009).
58. Arblaster, J. W. Crystallographic Properties of Iridium. *Platin. Met. Rev.* **54**, 93–102 (2010).
59. Murray, C. et al. Band bending and valence band quantization at line defects in MoS_2. *ACS Nano.* **14**, 9176–9187 (2020).
60. Lazić, P. CellMatch: Combining two unit cells into a common supercell with minimal strain. *Comput. Phys. Commun.* **197**, 324–334 (2015).
61. Giannozzi, P. et al. QUANTUM ESPRESSO: a modular and open-source software project for quantum simulations of materials. *J. Phys. Condens. Matter* **21**, 395502 (2009).
62. Berland, K. & Hyldgaard, P. Exchange functional that tests the robustness of the plasmon description of the van der Waals density functional. *Phys. Rev. B* **89**, 035412 (2014).
63. Le Quang, T. et al. Band-bending induced by charged defects and edges of atomically thin transition metal dichalcogenide films. *2D Mater.* **5**, 035034 (2018).
64. Liu, X. et al. Rotationally commensurate growth of MoS_2 on epitaxial graphene. *ACS Nano* **10**, 1067–1075 (2016).

Acknowledgements

We acknowledge D. Rybakowski for his technical support and drawings. The authors acknowledge funding from the Deutsche Forschungsgemeinschaft (DFG, German Research Foundation) within SPP 2196 (project number 423876021) and Marie Skłodowska-Curie Actions (MSCA) Postdoctoral Fellowship (project 101107288, 2D-InTune, B.P.). Co-authors from Zagreb acknowledge support by the Center of Excellence for Advanced Materials and Sensing Devices (Grant No. KK.01.1.1.01.0001) and Centre for Advanced Laser Techniques (Grant No. KK.01.1.1.05.0001) co-financed by the Croatian Government and the European Union through the European Regional Development Fund - Competitiveness and Cohesion Operational Program. D.N. acknowledges financial support from the Croatian Science Foundation (grant no. UIP-2019-04-6869).

Author contributions

B.P. conceptualization, synthesis, experimental characterization (STM, LEED, STS), analysis of the data, writing, discussing. M.M. DFT calculations, writing. D.N. conceptualization, DFT calculations, writing, writing-review. J.C. conceptualization, writing. A.B. synthesis, experimental characterization (STM, STS, LEED). R.O. experimental characterization (STS), reviewing, discussing. M.K. writing-review, discussing. I.Š.R. conceptualization, writing, discussing, writing-review. C.B. conceptualization, writing, discussing, writing-review.

Funding

Open Access funding enabled and organized by Projekt DEAL.

Competing interests

The authors declare no competing interests.

Additional information

Supplementary information The online version contains supplementary material available at https://doi.org/10.1038/s41699-024-00488-3.

Correspondence and requests for materials should be addressed to Borna Pielić or Iva Šrut Rakić.